catalysts

MDPI

Article

Highly Active Ag-Cu Nanocrystal Catalyst-Coated Brewer's Spent Grain Biochar for the Mineralization of Methyl Orange and Methylene Blue Dye Mixture

Lahcen Boubkr [1], Arvind K. Bhakta [1,2,*], Youssef Snoussi [1], Cora Moreira Da Silva [1], Laurent Michely [3], Mohamed Jouini [1], Souad Ammar [1,*] and Mohamed M. Chehimi [1,*]

[1] Université Paris Cité, CNRS, ITODYS, 75013 Paris, France
[2] Department of Chemistry, St. Joseph's University (Autonomous), Bangalore 560027, India
[3] Université Paris Est, CNRS, ICMPE (UMR 7182), 94320 Thiais, France
* Correspondence: arvind-kumar.bhakta@u-paris.fr (A.K.B.); ammarmer@univ-paris-diderot.fr (S.A.); mohamed.chehimi@cnrs.fr (M.M.C.)

Abstract: The aim of the present work is to valorise the brewing industry's waste, i.e., brewer's spent grain (BSG), into functional biocarbon for environmental catalysis applications. In this context, cost-effective and environmentally friendly biochar support coated with in-situ-generated Ag-Cu nanocrystals, was developed via the wet impregnation of BSG biomass powder with copper (II) nitrate trihydrate and silver nitrate aqueous solution prior to pyrolysis at moderate temperature (500 °C). Small-size homogenously distributed Ag-Cu nanocrystals (≤80 nm) on the surface of the biochar (Biochar@Ag-Cu) were observed by field emission scanning electron microscope (FESEM) and transmission electron microscope (TEM). Elemental compositions were determined by X-ray photoelectron spectroscopy (XPS) and energy dispersive X-ray analysis (EDX). The crystalline nature of the nanoparticles was confirmed by X-ray powder diffraction (XRD). Information about the thermal stability of the materials and quality were obtained by thermogravimetric analysis (TGA) and Raman, respectively. The potentiality of the Biochar@Ag-Cu catalyst in the field of pollutant removal is demonstrated by taking methyl orange and methylene blue as model dyes. A kinetics study was performed and analyzed by UV–vis spectroscopy. Its highly active catalytic nature is proved by the complete mineralization of the methyl orange dye (100%) through oxidative degradation. The reusability of the catalyst has shown 96% removal efficiency after 3 cycles. The linear plot of $-\mathrm{Ln}\,(C_A/C_0)$ vs. time ($R^2 = 0.9892$) reveals that the mineralization of the methyl orange dye follows pseudo-first-order kinetics ($k = 0.603 \times 10^{-2}\ \mathrm{min}^{-1}$). A methyl orange + methylene blue dye mixture degradation study has revealed the faster kinetics of the present catalyst towards methylene blue degradation. The current study suggests that BSG Biochar@Ag-Cu can be a potential candidate in contribution towards SDG 6.

Keywords: bimetallic catalysts; biochar; total dye mineralization; water treatment; brewing industry; waste to wealth

Citation: Boubkr, L.; Bhakta, A.K.; Snoussi, Y.; Moreira Da Silva, C.; Michely, L.; Jouini, M.; Ammar, S.; Chehimi, M.M. Highly Active Ag-Cu Nanocrystal Catalyst-Coated Brewer's Spent Grain Biochar for the Mineralization of Methyl Orange and Methylene Blue Dye Mixture. *Catalysts* **2022**, *12*, 1475. https://doi.org/10.3390/catal12111475

Academic Editors: Vitali A. Grinberg and Alexander D. Modestov

Received: 3 October 2022
Accepted: 14 November 2022
Published: 18 November 2022

1. Introduction

The carbon allotropes family is diversified with many fascinating structures and hybridisation [1]. The last two decades has witnessed the emergence of wonder nanomaterials such as carbon nanotubes [2], graphene [3], fullerene [4], carbon nano-horns, and nano-onions [5], which have been tested in numerous technologies such as water treatments, batteries, fuel cells, tissue engineering, pharmaceuticals, etc. [6].

However, with global environmental and climate change concerns, the focus is on the recycling and valorisation of waste [7]. Thus, it is no surprise that researchers are shifting their focus towards low-cost biochar [8–10], also coined "the new black" (https://www.sciencesetavenir.fr/nature-environnement/developpement-durable/biochar-le-nouvel-or-

noir_166521 last accessed 6 November 2022). It is basically derived from plant or animal waste and synthesised through a thermochemical process [11,12]. Their porosity, water-holding capacity, high surface area, pH and nutritious nature [13] make it applicable to plenty of different purposes, such as dye adsorption [14], filler in rubber composites [15], the recovery of sour anaerobic digesters [16] and engineering and agricultural applications [17], to mention a few.

Every year, plenty of dye effluents contaminate water bodies. A cationic dye, methylene blue (MB), and an anionic dye, methyl orange (MO), have been studied as model pollutants [18]. The sources of the dyes are textiles, leather, plastics, pharmaceuticals, paper industries, etc. [19–21]. MB exposure may cause burning sensations, nausea, breathing difficulties, diarrhoea and vomiting. Large doses can even cause severe headaches, mental confusion, chest pains and methemoglobinemia [22,23]. The dyes are genotoxic, mutagenic and carcinogenic as well as a big threat to aquatic life [24]. There are different methods of water treatment, such as adsorption [25–28], degradation [29], mineralisation [30], coagulation [31], sedimentation, and ion exchange processes [32]. Though adsorption is a low-cost energy process, the fate of molecules after adsorption is still challenging. Just normal degradation can remove the primary molecules; however, the degraded product can be either toxic or non-toxic [33]. In contrast, total mineralization removes all the organic parts and results in purified water [34].

Silver (Ag) nanoparticles are well known for their antibacterial, anti-fungal, antioxidant, anti-fouling, anti-cancer, anti-viral, anti-quorum sensing, anti-angiogenic, anti-inflammatory, anti-proliferative [35,36], and osteogenic properties [37]. Silver-containing compounds or their hybrids possess catalytic activity for dye degradation [38,39]. Copper nanoparticles also exhibit antibacterial, antioxidant and anti-diabetic activity [40] as well as being heterogeneous Fenton-like catalysts [41]. It is no surprise that working with bimetallic nanoparticles results in the synergistic effects of both nanoparticles in a single nanocomposite [42]. Recent studies have found that copper-containing Ag composites are very efficient and effective in the degradation of water effluents [43]. Ag-Cu nanoparticles are applicable for dye degradation by oxidative or reductive degradation for both cationic or anionic dyes [44]. Thus, Ag brings antibacterial and catalytic properties and their activity is further enhanced by Cu incorporation, which is a low-cost material compared to noble metals. Ag/Cu properties are tunable by doping with other nanoparticles [45,46].

Brewer's spent grain (BSG) is a by-product of the brewing industry. Its huge production is an opportunity for biomass waste valorization and, thus, a contribution towards a circular economy [47,48]. They are utilized for animal feed, biogas production, etc. This is also an exciting opportunity to exploit BSG for utilization in producing biochar [49,50]. Biochar can act as a catalyst as it has rich functional groups and a good porous structure [51]. Furthermore, impregnating biochar with catalytic nanoparticles improves its catalytic efficiency in water purification. Hence, we used wet chemical synthesis [42,52] to obtain homogeneous small-sized nanoparticles on biochar.

In the literature, there are some methods reported to coat biochar with Ag-Cu bimetallic nanoparticles. Snoussi et al. [53] used arylated biochar (SO_3H-biochar) to disperse Ag-Cu nanoparticles on their surface via the reduction of silver and copper ions using natural extracts. Hosny et al. [54] reported on the preparation of biochar using *Atriplex halimus* biomass, followed by modification with AgNPs and CuNPs. *A. halimus* was used as a stablising and reducing agent. Wang et al. used Ag/Cu_2O/cotton fabric for the treatment of dye wastewater [55]. Cu-Ag/C was also utilized for the hydroxylation of benzene (HOB) [56].

A thorough literature survey has revealed that there is not even a single work on copper silver bimetallic particle/biochar composites for the degradation of methyl orange (Figure 1). As a matter of fact, we have gone through several combinations or sequences of keywords using the Web of Science search engine to look for the most relevant papers, but no close or relevant results were returned by this important database. Hence, we were motivated to impregnate copper and silver nanoparticles on brewer' spent grain biochar

via a simple and reproducible wet impregnation technique. MO and MB dyes were taken as model pollutants [57] to test the catalytic activity towards dye degradation. The present material can be a potential candidate for environmental applications. Ultimately, the aim of the present work is to contribute towards Sustainable Development Goal (SDG) 6 [58].

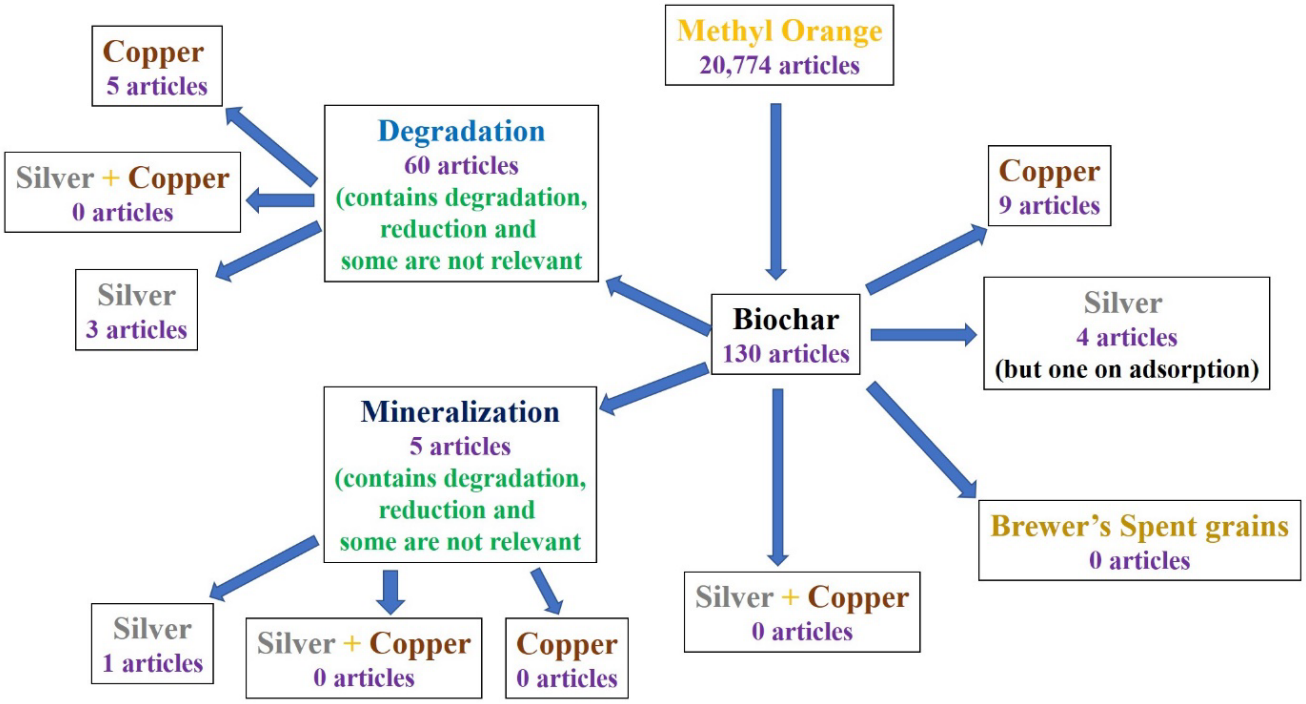

Figure 1. Literature survey of work related to biochar, copper, silver and methyl orange (source: Web of Science, dated 5 September 2022).

2. Results and Discussion

The sample was characterized using different techniques. It is noted that the untreated biochar, biochar coated with Ag, biochar coated with Cu and biochar coated with Ag-Cu are abbreviated as Biochar, Biochar@Ag, Biochar@Cu and BiocharAg-Cu, respectively.

2.1. Crystallinity of the Material

Figure 2 depicts the XRD spectra of different biochar samples. In all the cases, the peaks at 2θ = 50.8 and 59.4 are ascribed to the Cu (111) and Cu (002) planes (reference code 98-062-7113) [59] in the sample Biochar@Cu (Figure 2d), respectively. The peak in sample Biochar@Ag (Figure 2c) at 2θ = 44.8, 52.0 and 76.7 are due to the planes Ag (111), Ag (002) and Ag (022) (reference code 98-005-3759) [60]. These characteristic peaks of both Ag and Cu are present in the sample Biochar@Ag-Cu (Figure 2b), representing the successful impregnation of the biochar with Ag-Cu nanoparticles (reference code 98-060-4104) [61]. One can note that there are clear, distinct phases, Cu and Ag. Note that the Ag diffraction peaks appear broader in the Biochar@Ag sample compared to the Biochar@Ag-Cu sample. It may or may not be a kind of core (Ag)–shell (Cu) particle, where copper precipitation limits Ag growth. This is also supported by the fact that the copper signal is more intense than that of silver in the Biochar@Ag-Cu sample.

2.2. Surface Chemical Composition of the Catalyst

XPS characterisation was carried out to understand the chemical composition of the sample. It is obvious that just the biochar sample lacks Ag and Cu. Further, when it is coated with Ag or Cu or Ag-Cu, it is clearly found in the XPS survey spectra (Figure 3). The surface composition (in atomic percentage) is reported in Table 1. In the sample Biochar@Ag-Cu, the percentage of Ag and Cu are 0.4 and 0.7, respectively.

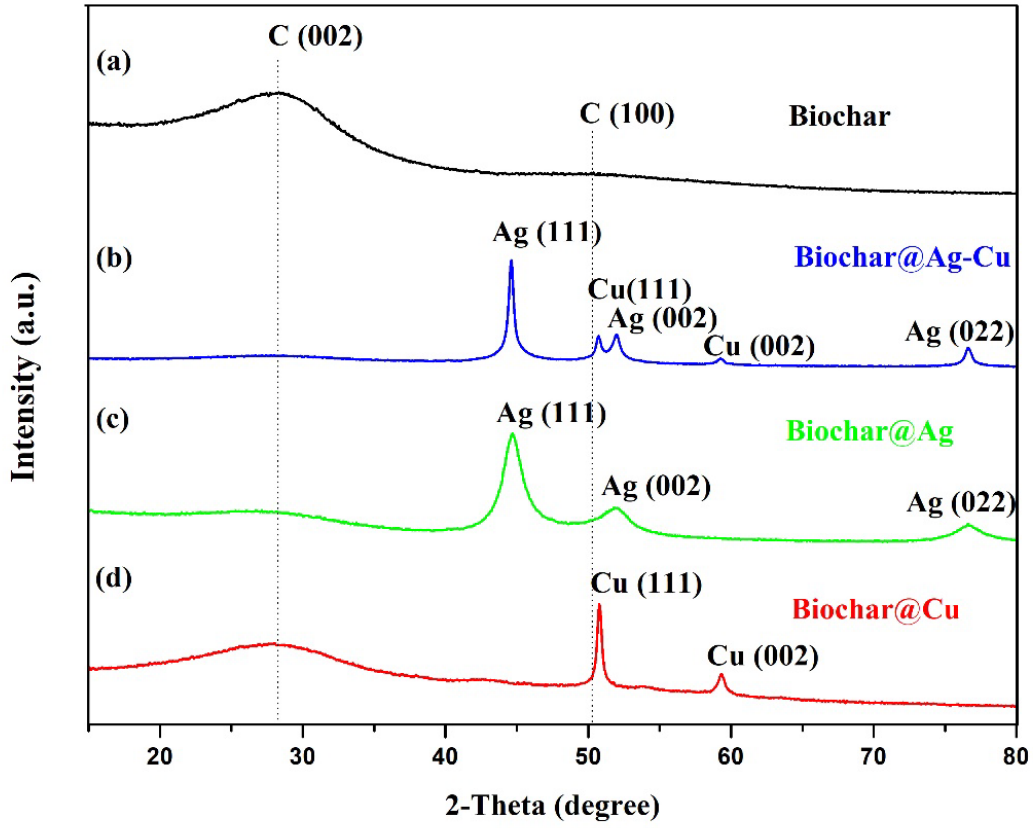

Figure 2. XRD patterns of (**a**) Biochar, (**b**) Biochar@Ag-Cu, (**c**) Biochar@Ag and (**d**) Biochar@Cu.

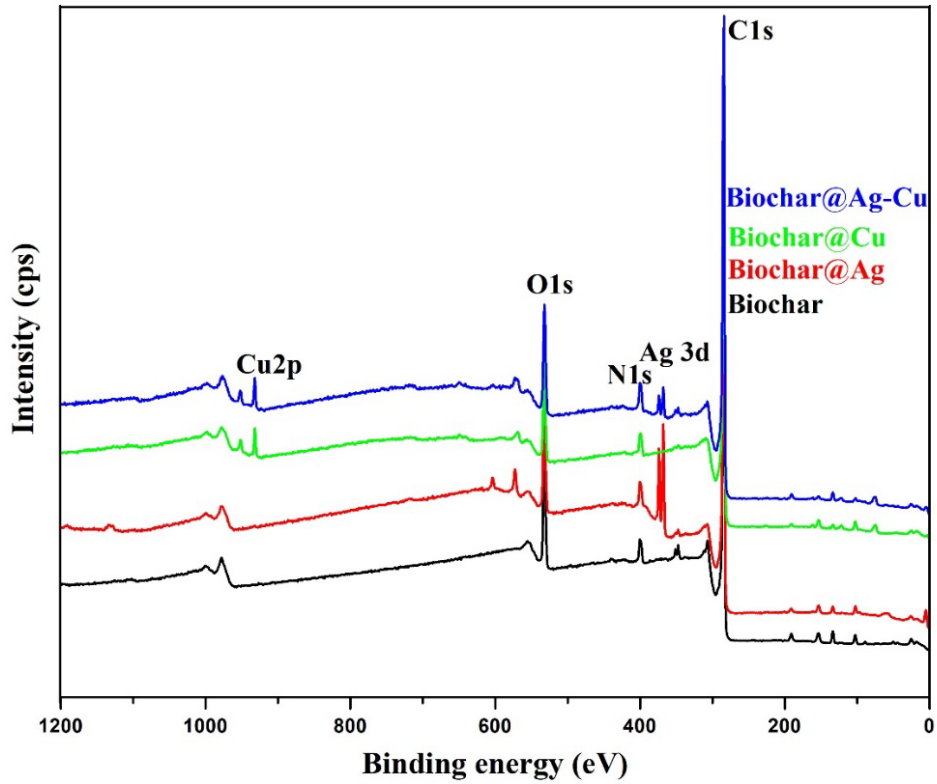

Figure 3. XPS survey scans of biochar and nanoparticle-decorated biochar.

Table 1. XPS atomic% composition of biochar and nanoparticle-impregnated biochar.

Sample	C	O	Cu	Ag	S	N	P	Si	Ca	Mg
Biochar	78.5	12.6	-	-		3.7	1.6	2.0	0.8	0.8
Biochar@Ag	80.3	10.8	-	1.3	0.1	4.3	1.0	1.5	0.4	0.4
Biochar@Cu	82.7	9.4	0.5	-	0.2	3.8	0.6	1.9	0.3	0.5
Biochar@Ag-Cu	81.7	9.8	0.7	0.4	0.2	4.5	1.1	0.6	0.5	0.5

The high-resolution spectra of Ag3d (Figure 4a) indicate that the silver is in a metallic state [62]. Figure 4b is also an indication of Cu in the metallic state, but of course, due to the very reactive nature of the nanoparticles, slight oxidation cannot be neglected [63–65]. Interestingly, the absence of the shake-up satellite peak in the Cu2p region suggests that copper nitrate has been completely reduced to the metallic state [66]. The pyrrolic and pyridinic [67] components of N1s are clearly seen in Figure 4c. It is likely that these nitrogen-containing species contribute to the tight immobilization of the metallic nanoparticles on the biochar.

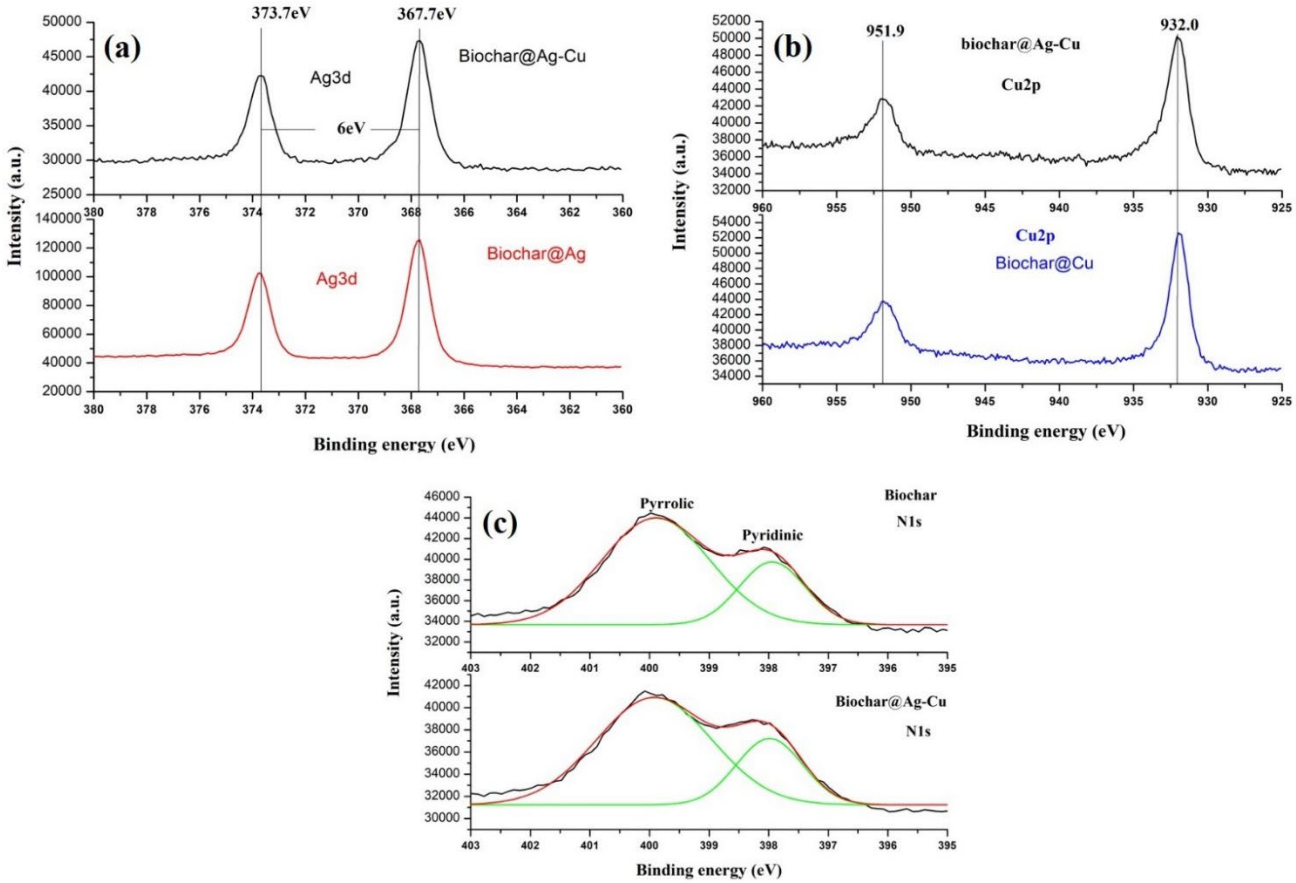

Figure 4. High-resolution spectra of (**a**) Ag3d of Biochar@Ag-Cu and Biochar@Ag, (**b**) Cu2p of Biochar@Ag-Cu and Biochar@Cu, and (**c**) N1s peak of Biochar and Biochar@Ag-Cu.

2.3. Surface Morphology of the Material and Bulk Composition

The study of the surface morphology of the biochar and the nanoparticle-impregnated biochar was carried out by FESEM, as shown in Figure 5. It is quite obvious that the surface of the pristine biochar (Figure 5a) is smoother compared to one with the presence of nanoparticles (Figure 5b–d). It is observed that the biochar impregnated with Cu nanoparticles (Figure 5c) is of slightly larger size compared to biochar with Ag nanoparticles (Figure 5b). The Ag-Cu nanoparticle (Figure 5d) size ($\leq$80 nm) is in between the Ag and Cu nanoparticles. In all cases, the shape of the nanoparticles is quasi-spherical. The distribution

of Ag nanoparticles and Ag-Cu on biochar is much better than just Cu nanoparticles. The homogeneity and dispersibility of nanoparticles on the biochar surface is a clear indication of efficient methodology. The current method is simple and avoids multistep procedures and the use of stabilising and reducing agents [54,68]. This also means that biochar derived from Brewer's spent grains is an excellent support to disperse Ag-Cu nano-catalysts on its surface compared to another biomass-derived biocarbon. In addition, the support is very necessary to avoid particle agglomeration, as reported in the literature [69]. EDX mapping is provided in Figure 6. This indicates the uniform distribution of the probed elements, signifying that the biochar samples are homogeneous. The atomic percentage compositions obtained from EDX mapping are as follows: C (79.43 %), N (4.85%), O (10.49%), Mg (0.58%), Si (0.14%), P (1.84%), S (0.22%), Ca (0.46%), Cu (1.14 %) and Ag (0.85%). Furthermore, these entire biomass-derived carbon materials should be characterised by a CHNS elemental analyser for more accurate measurements. This will give an idea about the correlation between the pyrolysis temperature and the H/C atomic ratio [70].

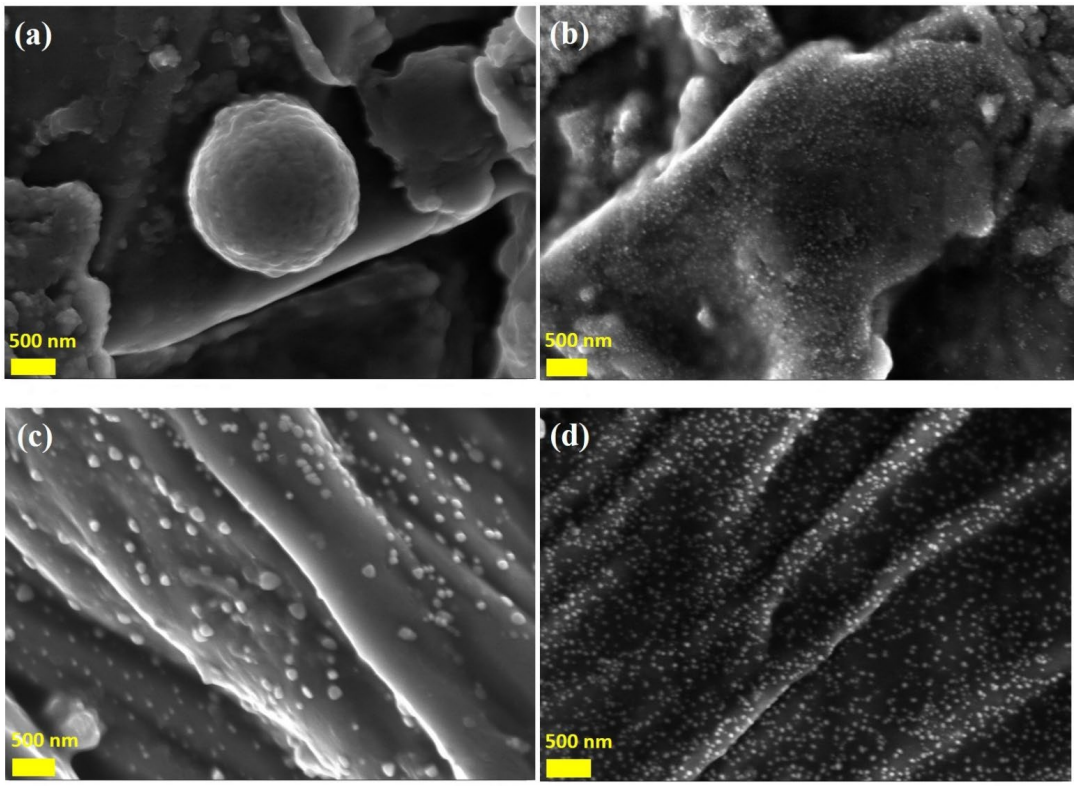

Figure 5. FESEM images of (**a**) Biochar, (**b**) Biochar@Ag, (**c**) Biochar@Cu and (**d**) Biochar@Ag-Cu.

The TEM images are displayed in Figure 7. Figure 7a–c depict the small-size nature of the nanoparticles, which are homogeneously distributed over the biochar surface. Particle sizes are mostly less than 50 nm, but sometimes, larger ones are found. Figure 7d shows the lamellar arrangements. The clear morphology of the nanoparticle, which was in association with biochar, was difficult to observe, so some spots were found where some free nanoparticles were present (Figure 7e). The presence of free nanoparticles can be due to the strong sonication used to disperse Biochar@Ag-Cu in ethanol for drop casting on the TEM grid. Different kinds of shapes of nanoparticles exist. Here, particle phase segregation exists. This image (Figure 7e) also highlights the occurrence of moires. Moires are the formation of fringes generated by interference between periodic elements or the superposition of the interference images of crystals with different orientations or inter-reticular distances (d_{hkl}) [71]. Selected area electron diffraction (SAED) patterns (Figure 7f) show d_{hkl} 0.239 (111), 0.210 (200) and 0.147(220) correspond to Ag with a lattice parameter expansion of 1.80% (0.416 +/− 0.004 nm) and d_{hkl} 0.210 (111), 0.187 (200), and 0.130 (220)

are related to Cu [72–74], with a lattice parameter expansion of 2.2 % (0.370 +/− 0.005 nm). The SAED patterns also reveal the crystalline nature of the nanoparticles.

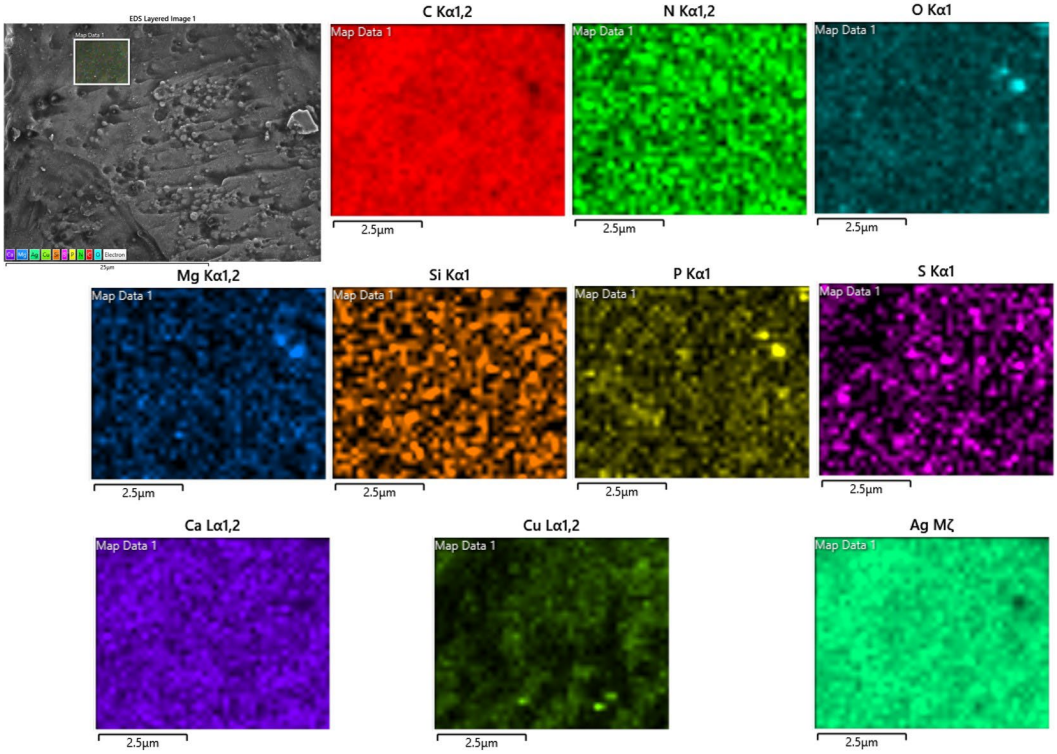

Figure 6. EDX mapping of Biochar@Ag-Cu.

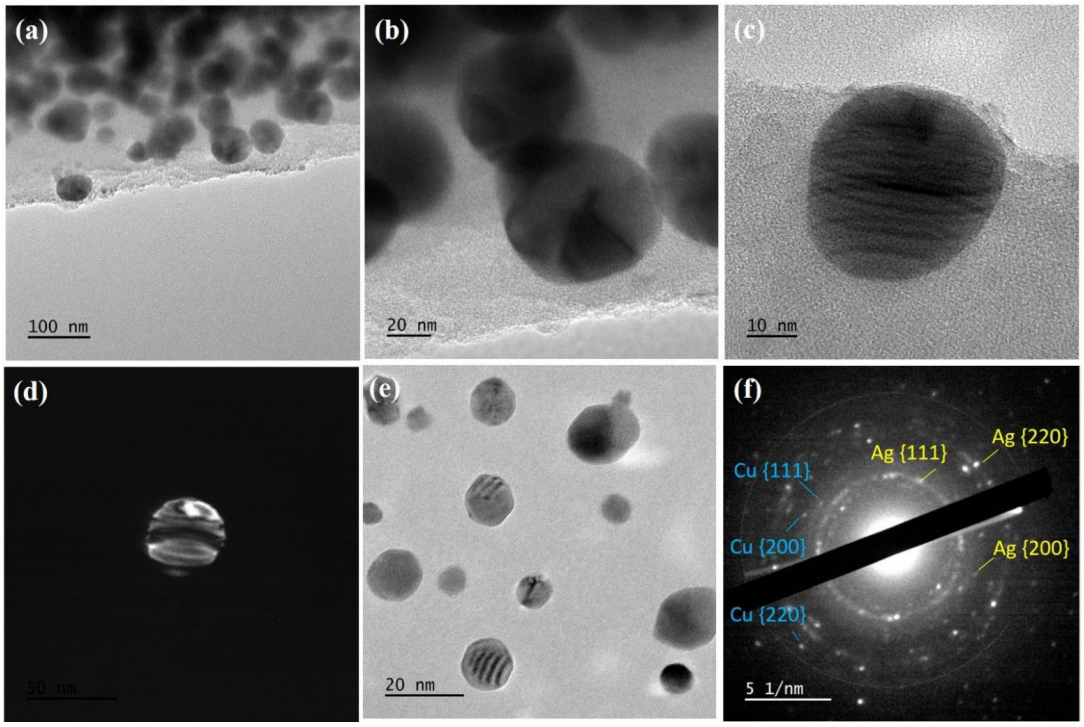

Figure 7. TEM micrographs (**a**–**c**) in the bright-field mode of Biochar@Ag-Cu at different resolutions: (**d**) in the dark field mode on Ag (111) showing the lamellar arrangements, (**e**) in the bright-field mode of free nanoparticles showing Moire figures, and (**f**) SAED patterns of nanoparticle assembly.

2.4. Study of the Degree of Graphitization

Raman characterisation was performed in order to understand the purity of the sample and the extent of graphitisation [75,76]. The curve fitting of Raman spectra (Figure 8) shows mostly six peaks: D (heteroatoms and defects), G (extent of graphitization), S_L (hydrogen circulation along periphery), GL (carbonyl function), V (sp^2-C) and S (alkyl-alkyl ether) [77–79]. It is noticed from the Raman analysis that decoration with Ag-Cu resulted in broad peaks as well as an increase in alkyl-alkyl ether functionalities. The metal-induced enhanced graphitization of biochar was reported elsewhere [53,80] and is consistent with the findings reported herein.

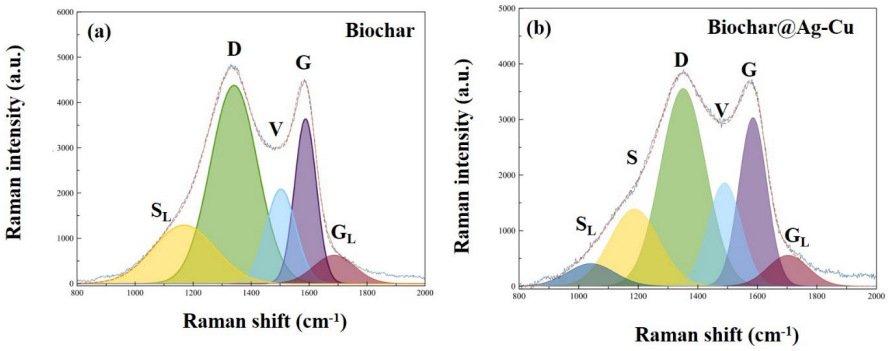

Figure 8. Raman spectra of (**a**) Biochar and (**b**) Biochar@Ag-Cu.

2.5. Thermal Stability

The thermogram of different biochar samples is given in Figure 9. It is found that the thermal stability of the material decreases with the presence of nanoparticles, which catalyses the decomposition. The higher the activity of the catalyst, the more it facilitates the decomposition of the biochar. The maximum effect is observed with Ag-Cu (Figure 9d). This can also be a sign of the high catalytic activity of Ag-Cu compared to just Ag and Cu. Further, the weight % remaining after 700 °C (Figure 9d) is also more (36% approx.) compared to Biochar@Ag (27%), Biochar@Cu (25% approx.) and Biochar (20% approx.). This phenomenon can be explained based on the fact that the formation of silver and copper oxides has high stability (oxidation of Ag and Cu occurs under air after heating during TGA analysis). Finally, the results are supported by the DTG curve [81], as shown in Figure 10, where T_{mwl} (temperature of maximum weight loss rate) [82] is lowest (398 °C) for Biochar@Ag-Cu and highest for just Biochar (602 °C), indicating they are the least and most stable, respectively. Based on this, the stability order is as follows: Biochar@Ag-Cu < Biochar@Cu < Biochar@Ag < Biochar.

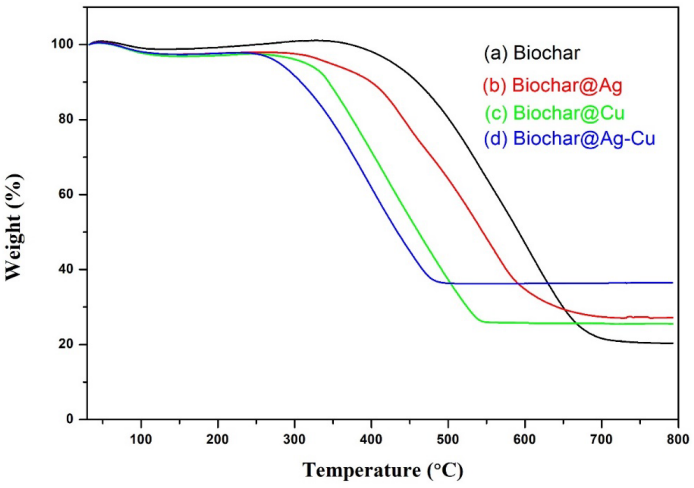

Figure 9. TGA curve of (**a**) Biochar, (**b**) Biochar@Ag, (**c**) Biochar@Cu and (**d**) Biochar@Ag-Cu.

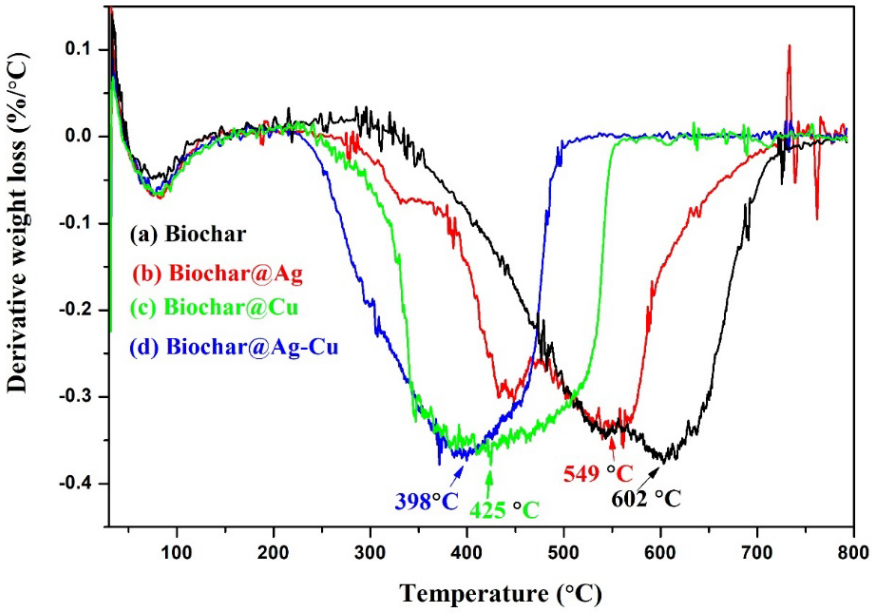

Figure 10. DTG curve of (a) Biochar, (b) Biochar@Ag, (c) Biochar@Cu and (d) Biochar@Ag-Cu.

2.6. Dye Degradation

The applicability of the present catalyst in the field of dye degradation is demonstrated by taking MO and MB dyes as model pollutants. The mechanism of MO dye degradation is given in Figure 11 [33,83]. It is found that after 6 h, MO is completely mineralized (Figure 12), which results in completely colourless water, resembling drinkable water, as shown in Figure 13.

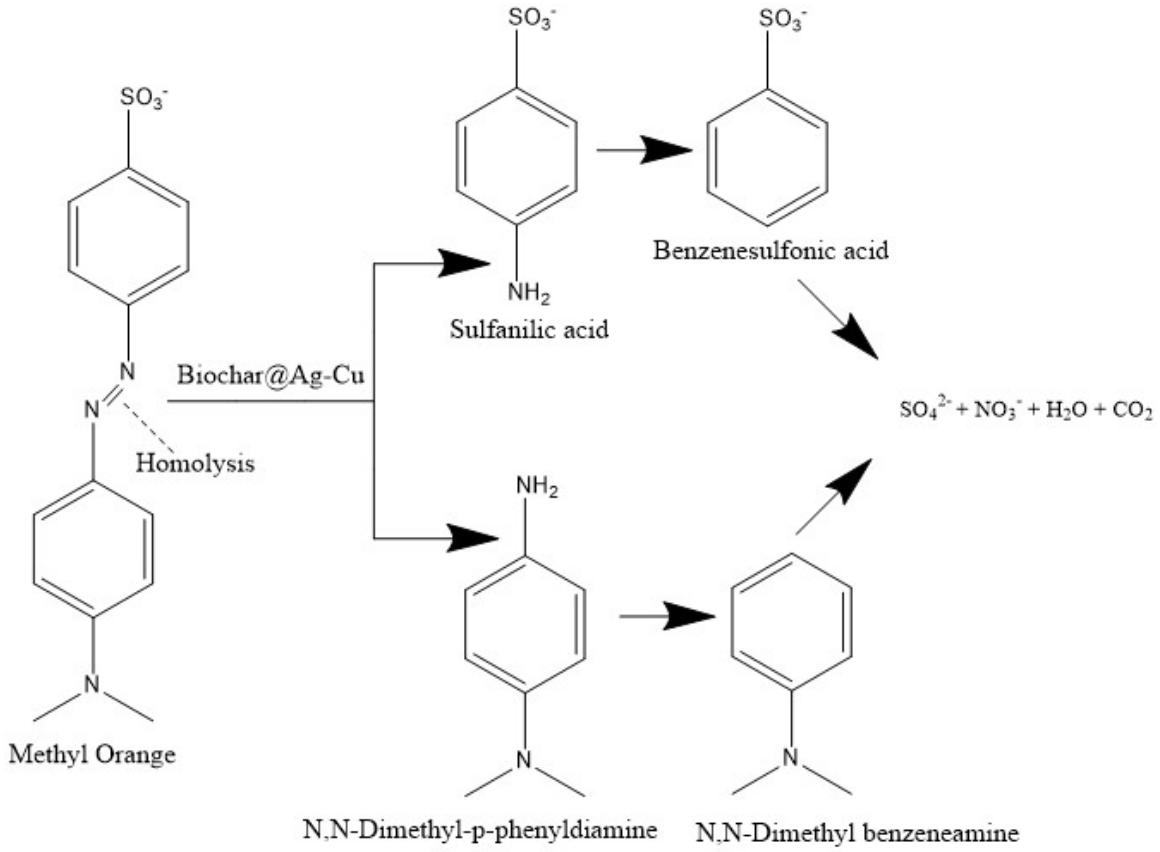

Figure 11. Mechanism of methyl orange dye mineralization.

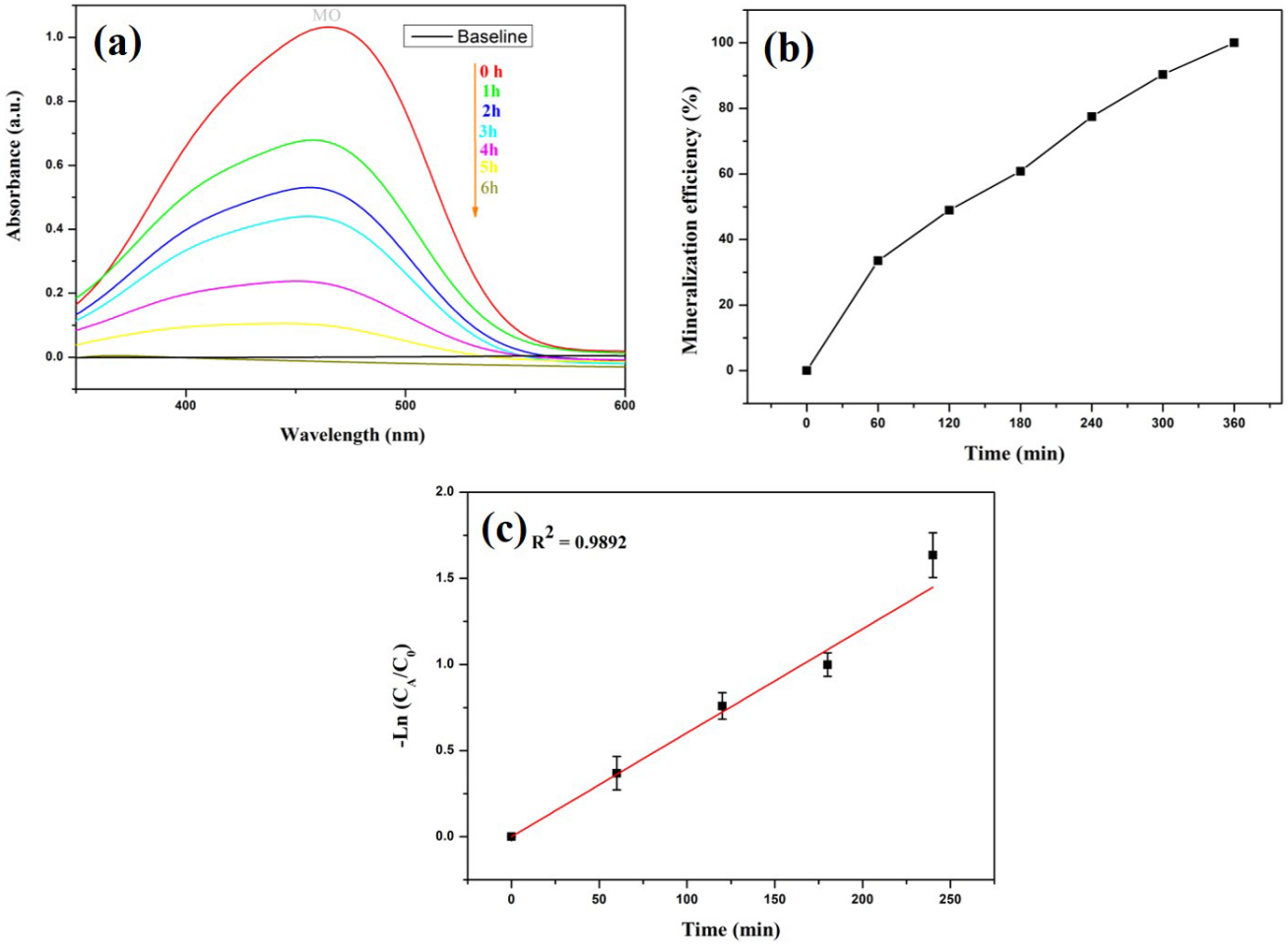

Figure 12. (**a**) UV–visible spectrum at different intervals of time: 10 ml of 20 ppm MO + 2 mL H_2O_2 + 5 mg of Biochar@Ag-Cu, (**b**) plot of mineralization efficiency, and (**c**) linear plot of -Ln (C_A/C_0) vs. time.

Figure 13. Colour of MO dye after 0 to 6 h of catalyst treatment in the presence of H_2O_2.

MO dye mineralization efficiency reaches 100% after 6 h of catalytic treatment in the presence of H_2O_2 (Figure 12a,b). Although UV–vis studies show no sign of a degradation product, the confirmation of complete mineralisation is best provided by total organic carbon (TOC) content measurements [84,85]. A study on the reusability of the catalyst was carried out. After three cycles, the percentage removal efficiency was found to be as high

as 96%. The plot of $-\mathrm{Ln}\,(C_A/C_O)$ vs. time (Figure 12c) follows a linear relationship with $R^2 = 0.9892$ and indicates it follows a pseudo-first-order model, as shown below:

$$\mathrm{Ln}\frac{[C]t}{[C]0} = -\mathrm{Kt} \quad (1)$$

Considering the pseudo-first-order model reaction, where K is the apparent rate constant (min^{-1}), $[C]_0$ = the initial concentration (mgL^{-1}) and $[C]_t$ = the concentration at time "t" (mgL^{-1}).

The comparison of mineralisation efficiency, with and without catalysts and H_2O_2, is also shown in Figure 14. It is noticed that the best performance is observed with Biochar@Ag-Cu in association with H_2O_2. A mixture of methyl orange and methylene blue solutions revealed that the present catalyst shows faster kinetics for methylene blue degradation than methyl orange degradation (Figure 15).

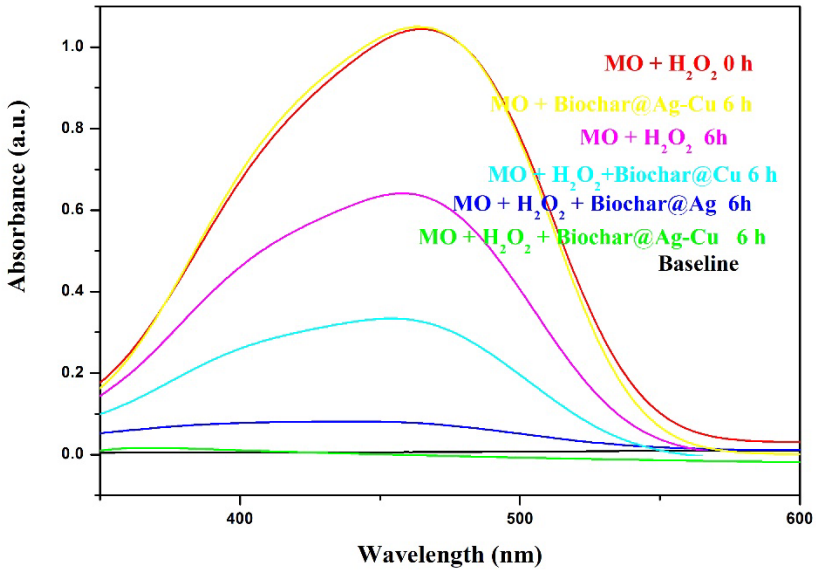

Figure 14. UV–vis spectra of MO after treatment with different catalysts.

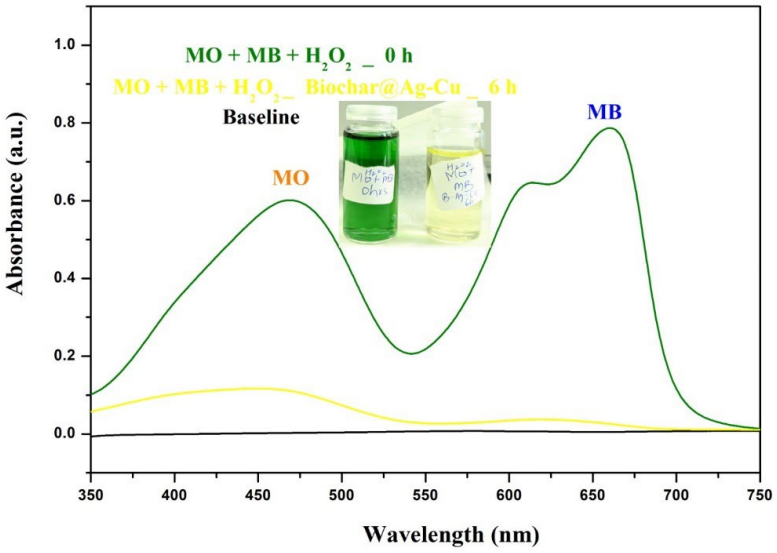

Figure 15. UV–visible spectra of a mixture of 5 mL of the MO solution (20 ppm, 6.1100×10^{-5} M), 5 mL of the MB solution (20 ppm, 6.2529×10^{-5} M), and 2 mL H_2O_2 at 0 h and 6 h after treatment with Biochar@Ag-Cu.

Table 2 compares different methods for MO degradation and their efficiency. It is found that the current method is highly attractive and cost-effective as it provides higher performances over other methods in terms of mineralisation efficiency, owing to the simple catalyst preparation method and operation under daylight exposure. More importantly, there is not even a single study on brewer's spent grain Biochar@Ag-Cu for methyl orange degradation. Thus, the current material may have high potential in the field of water treatment, particularly for removing pollutants released from the textile industry.

Table 2. Comparison of the catalytic performance of composite catalysts for the degradation of methyl orange reported in the literature with the current work.

Source of Support	Composite Catalyst	Fabrication Method and Characteristics of Materials	Light Source	Mineralisation Efficiency (%)	Ref.
Periodic mesoporous Organo silicate	Ag-/ZnO-PMOS	T-80 template assisted, sonication and use of $LiAlH_4$ as reducing agent.	Visible light	Degradation = 81%	[86]
Walnut shells	Ag/TiO_2/biochar	Mixing, calcination, and photo-deposition (three-step process)	500 W mercury-vapor lamp (λ = 360 nm)	85.38%	[87]
Walnut shells	TiO_2/ biochar	Hydrolysis method (two-step), large particles size due to agglomeration	UV irradiation	83.23%	[88]
Peanut shell	$HC/BiOBr/Bi_{12}TiO_2$	Hydrothermal (use of organic solvent)	7 W-LED (λ range = 380–780 nm)	Degradation efficiency = 16.67%	[89]
Olive pit	B-CA@CuNi	Wet impregnation	Daylight	Degradation efficiency = 75%	[42]
Potato straw	$MnFe_2O_4$/chitosan/biochar	Chemical co-precipitation method (multistep process and time-consuming)	Visible LED light/H_2O_2	99.50%	[90]
Brewer's spent grain	Biochar @AgCu (Ag:Cu = 1:1)	Wet impregnation (One pot)	Daylight/H_2O_2	100%	This work

3. Materials and Methods

3.1. Chemicals

Distilled water was used for all experimental purposes. Copper (II) nitrate trihydrate (99%) and silver nitrate (minimum 99.5%) were received from Acros organics and Rectapur (Geel, Belgium), respectively. BSG was obtained as a by-product of lager beer (it consists of a mixture of malts, i.e., barley and malt) from Belorge (Villers-sur-Mer, France). Hydrogen peroxide (30%) was purchased from Sigma-Aldrich, Burlington, VT, USA.

3.2. Apparatus

A coffee mill/grinder (Duronic, model: CG250, Voltage: 220–240 V, made in China) was used to grind the BSG biomass after washing and drying. FESEM was performed with emission current = 30µA and accelerating voltage = 5 kV (working distance = 6.9 mm). Firstly, a double-sided carbon tape is pasted on a sample holder to attach a cleaned silica plate. A biochar sample dispersed in ethanol via sonication is drop-casted on this silica plate and air-dried. This machine has an inbuilt EDX detector. WD was around 9 mm for the EDX analysis. TEM analysis was performed on JEOL TEM-2100 Plus electron microscope (Tokyo, Japan). Raman characterization was carried out on a Horiba HR 800 spectrometer (Kyoto, Japan). TGA characterisation was done in air, from RT to 800 °C, at a heating rate of 10 °C/min, using an HP DSC SETARAM SENSYS EVO (Caluire, France). XRD analysis was carried out on an X'Pert PRO PANalytical instrument (Cambridge, UK), where operating voltage and tube current were kept at 40 kV and 40 mA, respectively. XPS analysis was carried out using a Thermo Scientific K Alpha+ apparatus (Waltham, MA, USA) with the

pass energy of 200 and 80 eV for the survey scan (step size = 1 eV) and high-resolution spectra (step size = 0.1 eV), respectively. A UV–visible kinetic study was carried out using a Cary 4000 UV–vis spectrophotometer (SpectraLab Scientific Inc., Markham, ON, Canada).

3.3. Synthesis of Ag-Cu-Impregnated Biochar Catalyst

As-received brewer's spent grains were first washed with tap water (2 times) and distilled water (2 times). Then, it was dried in the oven at 150 °C for 4 h and 30 min. Later, it was ground using a coffee mill for 2 min [91]; 1 g of the BSG biomass powder was soaked in a copper (II) nitrate trihydrate solution (241.6 mg in 10 mL). In another experiment, 1 g of biomass powder was soaked in silver nitrate (169.8 mg in 10 mL distilled water). Lastly, 1 g of biomass powder was soaked in a copper (II) nitrate trihydrate (241.6 mg) and silver nitrate (169.8 mg) solution made to 10 mL. All three samples were dried in an oven at 60 °C overnight. After that, it was subjected to pyrolysis, with conditions as follows: type of method (P10 KOH Free), N_2 flow rate (1 L min^{-1}), ramp (20 °C min^{-1}), temperature (500 °C), residence time (1 h), and cooling time (1 h). This moderate-temperature pyrolysis method was applied to decrease the produced polycyclic aromatic hydrocarbons (PAHs). It is well known in the literature that synthesis at 500 °C causes biochar with lower PAH contents (483–2100 µg/Kg) [92]. Table 3 reports the % yield of the different biochar samples.

Table 3. % Yield of different biochar samples.

Sample Name	Weight before Pyrolysis (g)	Weight after Pyrolysis (g)	Percentage Yield
Biochar	3.145	0.896	28.5
Biochar@Cu	1.04	0.38	36.5
Biochar@Ag	0.98	0.41	41.8
Biochar@Ag-Cu	1.11	0.49	44.1

3.4. Dye Degradation Test

For the test, 5 mg of the catalyst was added to 10 mL of the 20 ppm MO solution. Further, 2 mL of H_2O_2 was added, and the solution was stirred for different intervals of time (1, 2, 3, 4, 5 and 6 h). A kinetics study was carried out using UV–visible spectroscopy. The test of the reusability of the catalyst was carried out by adding the same amount of MO solution and H_2O_2 in the same beaker. This was repeated until 3 cycles were completed. In the current work, we considered parameters such as the amount of the H_2O_2, catalyst (amount of catalyst and doping ratio), etc., to obtain the optimal conditions of degradation. As reported, a 6-hour duration was optimum for total mineralisation after trying at 1, 2, 3, 4, 5, and 6 h durations. The doping ratio of Cu and Ni was 1 mmole:1 mmole per 1 g of BSG powder. It is important to note, from our own experience and the ongoing research work, that increasing the loading of metal salts further is very likely to cause the agglomeration of the nanoparticles, hence increasing particle size and probably decreasing efficiency. Moreover, different pH conditions were not considered as our plan was to study only neutral pH for practical applications. For the effect of pH on dye mineralisation using biochar-based catalysts, the reader is referred to [93–95].

4. Conclusions

An efficient Ag-Cu nanoparticle-coated brewer's spent grain biochar has been developed via the wet impregnation method, followed by pyrolysis under an inert atmosphere at 500 °C. The composite catalyst and the related materials were characterised using several techniques. Although the current characterisation does not reveal carbide, the presence of carbide cannot be ignored. Nanoparticles mostly fall below 50 nm, but sometimes, bigger particles are also there. Current materials have been successfully used in depolluting water from harmful chemicals, such as MO by 100% ($k = 0.603 \times 10^{-2}$ min^{-1}), and also utilised to treat a MO and MB dye mixture. A reusability study has shown 96% MO removal efficiency after three cycles. Oxidative degradation has played an important role in achieving this

goal. A dye mixture degradation study has revealed the fast kinetics of MB degradation by catalyst compared to methyl orange. From the above, the methods reported in this work are simple, efficient and very easily reproducible. The Biochar@catalyst materials have a high potential in dye mineralisation, hence the interest in using them to treat textile industry wastewater. Particularly, brewer's spent grains can not only be used to feed farm animals (SDG 12: responsible consumption and production) but also be advantageously explored in designing high-performance catalysts. The BSG-based materials are, thus, expected to play an important role in the environmental sector and fulfil SDG 6.

Author Contributions: Conceptualization, A.K.B., Y.S. and M.M.C.; methodology, L.B., A.K.B., Y.S., M.J., S.A. and M.M.C.; validation, all authors; formal analysis, L.B., A.K.B., Y.S., L.M., C.M.D.S., S.A. and M.M.C.; investigation, L.B., A.K.B., Y.S., L.M., C.M.D.S., S.A. and M.M.C.; resources, S.A. and M.M.C.; data curation, A.K.B., Y.S. and M.M.C.; writing—original draft preparation, A.K.B.; writing—review and editing, all authors; visualization, A.K.B., Y.S. and M.M.C.; supervision, A.K.B., Y.S., M.J., S.A. and M.M.C.; project administration, A.K.B., S.A. and M.M.C.; funding acquisition, A.K.B., S.A. and M.M.C. All authors have read and agreed to the published version of the manuscript.

Funding: This research was funded by "Bourse Wallonie-Bruxelles International Excellence World (N° imputation—101386, and Article Budgetaire—33.01.00.07)". Financial support was also given by the French Ministry of Research, ANR (*Agence Nationale de la Recherche*), and CGI (*Commissariat à l'Investissement d'Avenir*) through a Labex SEAM (ANR-11-LABX-086, ANR-11-IDEX-0502) grant.

Data Availability Statement: Not applicable.

Acknowledgments: We would like to thank Benoit Boisanfray from Bel Orge brewery (located at 6 Rue des Grives, F-14640 Villers-sur-Mer, Calvados, Normandy, France) for providing us with the gift of brewer's spent grains. We are grateful to the experimental officers at the ITODYS lab for their assistance with Raman, FE-SEM/EDX, and XPS characterization.

Conflicts of Interest: The authors declare no conflict of interest. The funders had no role in the design of the study; in the collection, analyses, or interpretation of data; in the writing of the manuscript; or in the decision to publish the results.

References

1. Meunier, V.; Ania, C.; Bianco, A.; Chen, Y.; Choi, G.B.; Kim, Y.A.; Koratkar, N.; Liu, C.; Tascon, J.M.D.; Terrones, M. Carbon science perspective in 2022: Current research and future challenges. *Carbon N. Y.* **2022**, *195*, 272–291. [CrossRef]
2. Iijima, S. Helical microtubules of graphitic carbon. *Nature* **1991**, *354*, 56–58. [CrossRef]
3. Novoselov, K.S.; Geim, A.K.; Morozov, S.V.; Jiang, D.; Zhang, Y.; Dubonos, S.V.; Grigorieva, I.V.; Firsov, A.A. Electric Field Effect in Atomically Thin Carbon Films. *Science* **2004**, *306*, 666–669. [CrossRef] [PubMed]
4. Kroto, H.W.; Heath, J.R.; O'Brien, S.C.; Curl, R.F.; Smalley, R.E. C_{60}: Buckminsterfullerene. *Nature* **1985**, *318*, 162–163. [CrossRef]
5. Ugarte, D. Curling and closure of graphitic networks under electron-beam irradiation. *Nature* **1992**, *359*, 707–709. [CrossRef] [PubMed]
6. Sridharan, R.; Monisha, B.; Kumar, P.S.; Gayathri, K.V. Carbon nanomaterials and its applications in pharmaceuticals: A brief review. *Chemosphere* **2022**, *294*, 133731. [CrossRef] [PubMed]
7. Pandey, D.; Daverey, A.; Dutta, K.; Yata, V.K.; Arunachalam, K. Valorization of waste pine needle biomass into biosorbents for the removal of methylene blue dye from water: Kinetics, equilibrium and thermodynamics study. *Environ. Technol. Innov.* **2022**, *25*, 102200. [CrossRef]
8. Bhakta, A.K.; Fiorenza, R.; Jlassi, K.; Mekhalif, Z.; Ali, A.M.A.; Chehimi, M.M. The emerging role of biochar in the carbon materials family for hydrogen production. *Chem. Eng. Res. Des.* **2022**, *188*, 209–228. [CrossRef]
9. Azan, N.A.A.M.; Sagadevan, S.; Mohamed, A.R.; Azazi, A.H.N.; Suah, F.B.M.; Kobayashi, T.; Adnan, R.; Kaus, N.H.M. Solar Light-Induced Photocatalytic Degradation of Ciprofloxacin Antibiotic Using Biochar Supported Nano Bismuth Ferrite Composite. *Catalyst* **2022**, *12*, 1269. [CrossRef]
10. Ioannidi, A.A.; Vakros, J.; Frontistis, Z.; Mantzavinos, D. Tailoring the Biochar Physicochemical Properties Using a Friendly Eco-Method and Its Application on the Oxidation of the Drug Losartan through Persulfate Activation. *Catalyst* **2022**, *12*, 1245. [CrossRef]
11. Adeniyi, A.G.; Ighalo, J.O.; Onifade, D.V. Biochar from the thermochemical conversion of Orange (Citrus sinensis) peel and albedo: Product quality and potential applications. *Chem. Africa* **2020**, *3*, 439–448. [CrossRef]
12. Das, R.; Panda, S.N. Preparation and applications of biochar based nanocomposite: A review. *J. Anal. Appl. Pyrolysis* **2022**, *167*, 105691. [CrossRef]
13. Weber, K.; Quicker, P. Properties of biochar. *Fuel* **2018**, *217*, 240–261. [CrossRef]

14. Ali, Y.A.E.H.; Ahrouch, M.; Lahcen, A.A.; Abdellaoui, Y.; Stitou, M. Recent Advances and Prospects of Biochar-based Adsorbents for Malachite Green Removal: A Comprehensive Review. *Chem. Africa* **2022**. [CrossRef]
15. Greenough, S.; Dumont, M.-J.; Prasher, S. The physicochemical properties of biochar and its applicability as a filler in rubber composites: A review. *Mater. Today Commun.* **2021**, *29*, 102912. [CrossRef]
16. Aramrueang, N.; Zhang, R.; Liu, X. Application of biochar and alkalis for recovery of sour anaerobic digesters. *J. Environ. Manag.* **2022**, *307*, 114538. [CrossRef]
17. Harussani, M.M.; Sapuan, S.M. Development of Kenaf Biochar in Engineering and Agricultural Applications. *Chem. Africa* **2022**, *5*, 1–17. [CrossRef]
18. Kumar K, A.; Shobham; Panwar, J.; Gupta, S. One-pot synthesis of metal oxide-clay composite for the evaluation of dye removal studies: Taguchi optimization of parameters and environmental toxicity studies. *Environ. Sci. Pollut. Res.* **2022**. [CrossRef]
19. Shrestha, P.; Jha, M.K.; Ghimire, J.; Koirala, A.R.; Shrestha, R.M.; Sharma, R.K.; Pant, B.; Park, M.; Pant, H.R. Decoration of Zinc Oxide Nanorods into the Surface of Activated Carbon Obtained from Agricultural Waste for Effective Removal of Methylene Blue Dye. *Materials* **2020**, *13*, 5667. [CrossRef]
20. Blue, M.; Orange, M. Critical Review on the Photodegradation Ability of Graphene and its Derivatives against Malachite Green, Methylene Blue, and Methyl Orange. *Lett. Appl. NanoBioScience* **2023**, *12*, 1–30. [CrossRef]
21. Kotp, Y.H. Fabrication of cerium titanate cellulose fiber nanocomposite materials for the removal of methyl orange and methylene blue from polluted water by photocatalytic degradation. *Environ. Sci. Pollut. Res.* **2022**, *29*, 81583–81608. [CrossRef] [PubMed]
22. Othman, N.H.; Alias, N.H.; Shahruddin, M.Z.; Bakar, N.F.A.; Him, N.R.N.; Lau, W.J. Adsorption kinetics of methylene blue dyes onto magnetic graphene oxide. *J. Environ. Chem. Eng.* **2018**, *6*, 2803–2811. [CrossRef]
23. Ghosh, D.; Bhattacharyya, K.G. Adsorption of methylene blue on kaolinite. *Appl. Clay Sci.* **2002**, *20*, 295–300. [CrossRef]
24. Waghchaure, R.H.; Adole, V.A.; Jagdale, B.S. Photocatalytic degradation of methylene blue, rhodamine B, methyl orange and Eriochrome black T dyes by modified ZnO nanocatalysts: A concise review. *Inorg. Chem. Commun.* **2022**, *143*, 109764. [CrossRef]
25. Benjelloun, M.; Miyah, Y.; Bouslamti, R.; Nahali, L.; Mejbar, F.; Lairini, S. The Fast-Efficient Adsorption Process of the Toxic Dye onto Shells Powders of Walnut and Peanut: Experiments, Equilibrium, Thermodynamic, and Regeneration Studies. *Chem. Africa* **2022**, *5*, 375–393. [CrossRef]
26. Dabagh, A.; Bagui, A.; Abali, M.; Aziam, R.; Chiban, M.; Sinan, F.; Zerbet, M. Increasing the Adsorption Efficiency of Methylene Blue by Acid Treatment of the Plant Carpobrotus edulis. *Chem. Africa* **2021**, *4*, 585–598. [CrossRef]
27. Nazir, M.A.; Najam, T.; Zarin, K.; Shahzad, K.; Javed, M.S.; Jamshaid, M.; Bashir, M.A.; Shah, S.S.A.; Rehman, A.U. Enhanced adsorption removal of methyl orange from water by porous bimetallic Ni/Co MOF composite: A systematic study of adsorption kinetics. *Int. J. Environ. Anal. Chem.* **2021**. [CrossRef]
28. Rigueto, C.V.T.; Alessandretti, I.; da Silva, D.H.; Rosseto, M.; Loss, R.A.; Geraldi, C.A.Q. Agroindustrial Wastes of Banana Pseudo-stem as Adsorbent of Textile Dye: Characterization, Kinetic, and Equilibrium Studies. *Chem. Africa* **2021**, *4*, 1069–1078. [CrossRef]
29. Ajiboye, T.O.; Oyewo, O.A.; Marzouki, R.; Brahmia, A.; Onwudiwe, D.C. Synthesis of AgBiS2/gC3N4 and its application in the photocatalytic reduction of Pb (II) in the matrix of methyl orange, crystal violet, and methylene blue dyes. *Ceram. Int.* **2022**, *in press*. [CrossRef]
30. Stanley, R.; Jebasingh, J.A.; Vidyavathy, S.M.; Stanley, P.K.; Ponmani, P.; Shekinah, M.E.; Vasanthi, J. Excellent Photocatalytic degradation of Methylene Blue, Rhodamine B and Methyl Orange dyes by Ag-ZnO nanocomposite under natural sunlight irradiation. *Optik* **2021**, *231*, 166518. [CrossRef]
31. Luo, X.; Liang, C.; Hu, Y. Comparison of Different Enhanced Coagulation Methods for Azo Dye Removal from Wastewater. *Sustainability* **2019**, *11*, 4760. [CrossRef]
32. Mukherjee, A.; Goswami, N.; Dhak, D. Photocatalytic Remediation of Industrial Dye Waste Streams Using Biochar and Metal-Biochar Hybrids: A Critical Review. *Chem. Africa* **2022**. [CrossRef]
33. Kgatle, M.; Sikhwivhilu, K.; Ndlovu, G.; Moloto, N. Degradation Kinetics of Methyl Orange Dye in Water Using Trimetallic Fe/Cu/Ag Nanoparticles. *Catalysts* **2021**, *11*, 428. [CrossRef]
34. Dos Santos, A.J.; Sires, I.; Martínez-Huitle, C.A.; Brillas, E. Total mineralization of mixtures of Tartrazine, Ponceau SS and Direct Blue 71 azo dyes by solar photoelectro-Fenton in pre-pilot plant. *Chemosphere* **2018**, *210*, 1137–1144. [CrossRef]
35. Jeevanandam, J.; Krishnan, S.; Hii, Y.S.; Pan, S.; Chan, Y.S.; Acquah, C.; Danquah, M.K.; Rodrigues, J. Synthesis approach-dependent antiviral properties of silver nanoparticles and nanocomposites. *J. Nanostruct. Chem.* **2022**, *12*, 809–831. [CrossRef]
36. Snoussi, Y.; Sifaoui, I.; Khalil, A.M.; Bhakta, A.K.; Semyonov, O.; Postnikov, P.S.; Michely, L.; Pires, R.; Bastide, S.; Barroso, J.E.-P.; et al. Facile synthesis of silver decorated biochar as a novel and highly active biosourced anti-kinetoplastid agent. *Mater. Today Commun.* **2022**, *32*, 104126. [CrossRef]
37. Nazarov, D.; Ezhov, I.; Yudintceva, N.; Shevtsov, M.; Rudakova, A.; Kalganov, V.; Tolmachev, V.; Zharova, Y.; Lutakov, O.; Kraeva, L.; et al. Antibacterial and Osteogenic Properties of Ag Nanoparticles and Ag/TiO2 Nanostructures Prepared by Atomic Layer Deposition. *J. Funct. Biomater.* **2022**, *13*, 62. [CrossRef]
38. Mahmood, K.; Amara, U.; Siddique, S.; Usman, M.; Peng, Q.; Khalid, M.; Hussain, A.; Ajmal, M.; Ahmad, A.; Sumrra, S.H.; et al. Green synthesis of Ag@CdO nanocomposite and their application towards brilliant green dye degradation from wastewater. *J. Nanostruct. Chem.* **2022**, *12*, 329–341. [CrossRef]

39. Shahzad, K.; Hussain, S.; Nazir, M.A.; Jamshaid, M.; ur Rehman, A.; Alkorbi, A.S.; Alsaiari, R.; Alhemiary, N.A. Versatile Ag_2O and ZnO nanomaterials fabricated via annealed Ag-PMOS and ZnO-PMOS: An efficient photocatalysis tool for azo dyes. *J. Mol. Liq.* **2022**, *356*, 119036. [CrossRef]
40. Ameena, S.; Rajesh, N.; Anjum, S.M.; Khadri, H.; Riazunnisa, K.; Mohammed, A.; Kari, Z.A. Antioxidant, Antibacterial, and Anti-diabetic Activity of Green Synthesized Copper Nanoparticles of Cocculus hirsutus (Menispermaceae). *Appl. Biochem. Biotechnol.* **2022**, *194*, 4424–4438. [CrossRef]
41. Zhu, G.; Jin, Y.; Ge, M. Simple and green method for preparing copper nanoparticles supported on carbonized cotton as a heterogeneous Fenton-like catalyst. *Colloids Surfaces A Physicochem. Eng. Asp.* **2022**, *647*, 128978. [CrossRef]
42. Omiri, J.; Snoussi, Y.; Bhakta, A.K.; Truong, S.; Ammar, S.; Khalil, A.M.; Jouini, M.; Chehimi, M.M. Citric-Acid-Assisted Preparation of Biochar Loaded with Copper / Nickel Bimetallic Nanoparticles for Dye Degradation. *Colloids Interfaces* **2022**, *6*, 18. [CrossRef]
43. Arasi, K.; Arasu, S.; Raja, A.G.; Rajaram, R. Photocatalytic Degradation of Effluent water by CuO @ Ag Core—Shell Nanoparticles as Effective Catalyst under Irradiation of UV-light. *Mater. Today Proc.* **2022**, *68*, 556–563. [CrossRef]
44. Tantawy, H.R.; Nada, A.A.; Baraka, A.; Elsayed, M.A. Novel synthesis of bimetallic Ag-Cu nanocatalysts for rapid oxidative and reductive degradation of anionic and cationic dyes. *Appl. Surf. Sci. Adv.* **2021**, *3*, 100056. [CrossRef]
45. Passi, M.; Pal, B. Influence of Ag/Cu photodeposition on $CaTiO_3$ photocatalytic activity for degradation of Rhodamine B dye. *Korean J. Chem. Eng.* **2022**, *39*, 942–953. [CrossRef]
46. Dong, S.; Lian, X.; Chen, S.; Li, H.; Liu, E.; Xu, K. Kinetic analysis and mechanism study on the photocatalytic degradation of 2,4-dinitrophenylhydrazine over surface plasmonic Ag/Cu/TiO_2 composite. *React. Kinet. Mech. Catal.* **2021**, *134*, 485–499. [CrossRef]
47. Singh, E.; Mishra, R.; Kumar, A.; Shukla, S.K.; Lo, S.-L.; Kumar, S. Circular economy-based environmental management using biochar: Driving towards sustainability. *Process Saf. Environ. Prot.* **2022**, *163*, 585–600. [CrossRef]
48. Bolwig, S.; Mark, M.S.; Happel, M.K.; Brekke, A. Beyond animal feed? The valorisation of brewers' spent grain. In *From Waste to Value*; Taylor & Francis: Abingdon, UK, 2019; pp. 107–121.
49. Sieradzka, M.; Kirczuk, C.; Kalemba-rec, I.; Mlonka-m, A.; Magdziarz, A. Pyrolysis of Biomass Wastes into Carbon Materials. *Energies* **2022**, *15*, 1941. [CrossRef]
50. Gupta, R.; Pandit, C.; Pandit, S.; Gupta, P.K.; Lahiri, D.; Agarwal, D.; Pandey, S. Potential and future prospects of biochar-based materials and their applications in removal of organic contaminants from industrial wastewater. *J. Mater. Cycles Waste Manag.* **2022**, *24*, 852–876. [CrossRef]
51. Zhao, C.; Shao, B.; Yan, M.; Liu, Z.; Liang, Q.; He, Q.; Wu, T.; Liu, Y.; Pan, Y.; Huang, J.; et al. Activation of peroxymonosulfate by biochar-based catalysts and applications in the degradation of organic contaminants: A review. *Chem. Eng. J.* **2021**, *416*, 128829. [CrossRef]
52. Snoussi, Y.; Sifaoui, I.; El Garah, M.; Khalil, A.M.; Barroso, J.E.; Jouini, M.; Ammar, S.; Lorenzo-Morales, J.; Chehimi, M.M. Green, zero-waste pathway to fabricate supported nanocatalysts and anti-kinetoplastid agents from sugarcane bagasse. *Waste Manag.* **2023**, *155*, 179–191. [CrossRef]
53. Snoussi, Y.; El Garah, M.; Khalil, A.M.; Chehimi, M.M. Immobilization of biogenic silver-copper nanoparticles over arylated biochar from sugarcane bagasse: Method and catalytic performance. *Appl. Organomet. Chem.* **2022**, *36*, e6885. [CrossRef]
54. Hosny, M.; Fawzy, M.; Eltaweil, A.S. Phytofabrication of bimetallic silver-copper / biochar nanocomposite for environmental and medical applications. *J. Environ. Manag.* **2022**, *316*, 115238. [CrossRef]
55. Wang, L.; Mao, H.; Li, Z.; Wang, C.; Gao, D. Immobilizing Ag / Cu2O on cotton fabric to enhance visible light photocatalytic activity. *New J. Chem.* **2020**, *44*, 20759–20769. [CrossRef]
56. Tian, K.; Liu, W.; Zhang, S.; Jiang, H. One-pot synthesis of a carbon supported bimetallic Cu–Ag NPs catalyst for robust catalytic hydroxylation of benzene to phenol by fast pyrolysis of biomass waste. *Green Chem.* **2016**, *18*, 5643–5650. [CrossRef]
57. Al-qaradawi, S.; Salman, S.R. Photocatalytic degradation of methyl orange as a model compound. *J. Photochem. Photobiol. A Chem.* **2002**, *148*, 161–168. [CrossRef]
58. Ho, L.; Alonso, A.; Eurie Forio, M.A.; Vanclooster, M.; Goethals, P.L.M. Water research in support of the Sustainable Development Goal 6: A case study in Belgium. *J. Clean. Prod.* **2020**, *277*, 124082. [CrossRef]
59. Tokola, E.; Kantola, M. Annales Academiae Scientiarum Fennicae. *Ser. A6 Phys.* **1967**, *223*, 1–10.
60. Vegard, L. Vega. *Phys. Rev.* **1922**, *20*, 424–432.
61. Weibo, L.; Yinghong, Z.; Junqin, L. No Title. *J. Alloys Compd.* **1993**, *191*, 187–189.
62. Maria Ferraria, A.; Patrícia Carapeto, A.; do Rego, A.M. X-ray photoelectron spectroscopy: Silver salts revisited. *Vacuum* **2012**, *86*, 1988–1991. [CrossRef]
63. Biesinger, M.C. Advanced analysis of copper X-ray photoelectron spectra. *Surf. Interface Anal.* **2017**, *49*, 1325–1334. [CrossRef]
64. Biesinger, M.C.; Lau, L.W.M.; Gerson, A.R.; Smart, R.S.C. Applied Surface Science Resolving surface chemical states in XPS analysis of first row transition metals, oxides and hydroxides: Sc, Ti, V, Cu and Zn. *Appl. Surf. Sci.* **2010**, *257*, 887–898. [CrossRef]
65. Biesinger, M.C.; Hart, B.R.; Polack, R.; Kobe, B.A.; Smart, R.S.C. Analysis of mineral surface chemistry in flotation separation using imaging XPS. *Miner. Eng.* **2007**, *20*, 152–162. [CrossRef]
66. Almheiri, S.; Ahmad, A.A.L.; Le Droumaguet, B.; Pires, R.; Mohamed, A.A.; Chehimi, M.M. Development of Latent Fingerprints via Aryldiazonium Tetrachloroaurate Salts on Copper Surfaces: An XPS Study. *Langmuir* **2020**, *36*, 74–83. [CrossRef]

67. Kabir, S.; Artyushkova, K.; Serov, A.; Kiefer, B.; Atanassov, P. Binding energy shifts for nitrogen-containing graphene-based electrocatalysts—Experiments and DFT calculations. *Surf. Interface Anal.* **2016**, *48*, 293–300. [CrossRef]
68. Saad, A.G.; Gebreil, A.; Kospa, D.A.; El-Hakam, S.A.; Ibrahim, A.A. Integrated solar seawater desalination and power generation via plasmonic sawdust-derived biochar: Waste to wealth. *Desalination* **2022**, *535*, 115824. [CrossRef]
69. Yin, C.; Khan, A.; Gao, Q.; Li, Q.; Zhou, X.; Liu, X.; Xu, A.; Li, X. Synergistic activation of peroxymonosulfate for efficient aqueous p -nitrophenol degradation with Cu (II) and Ag (I) in $Ag_2Cu_2O_3$. *Sep. Purif. Technol.* **2022**, *291*, 120934. [CrossRef]
70. Xiao, X.; Chen, Z.; Chen, B. H/C atomic ratio as a smart linkage between pyrolytic temperatures, aromatic clusters and sorption properties of biochars derived from diverse precursory materials. *Sci. Rep.* **2016**, *6*, 22644. [CrossRef]
71. Fulong, D.; Yongrning, X. Nano-moire method. *ACTA Mech. Sin.* **1999**, *15*, 283–288. [CrossRef]
72. Dou, Q.; Li, Y.; Wong, K.W.; Ng, K.M. Facile synthesis of nearly monodisperse AgCu alloy nanoparticles with synergistic effect against oxidation and electromigration. *J. Mater. Res.* **2019**, *34*, 2095–2104. [CrossRef]
73. Fodjo, E.K.; Canlier, A.; Kong, C.; Yurtsever, A.; Guillaume, P.L.A.; Abe, M.; Patrice, F.T.; Tohei, T.; Sakai, A. Facile Synthesis Route of Au-Ag Nanostructures Soaked in PEG. *Adv. Nanopart.* **2018**, *7*, 37–45. [CrossRef]
74. Korneva, A.; Straumal, B.; Kilmametov, A.; Chulist, R.; Cios, G.; Baretzky, B.; Zięba, P. Dissolution of Ag Precipitates in the Cu–8wt.% Ag Alloy Deformed by High Pressure Torsion. *Materials* **2019**, *12*, 447. [CrossRef]
75. Tran, H.N.; Tomul, F.; Ha, N.T.H.; Nguyen, D.T.; Lima, E.C.; Le, G.T.; Chang, C.-T.; Masindi, V.; Woo, S.H. Innovative spherical biochar for pharmaceutical removal from water: Insight into adsorption mechanism. *J. Hazard. Mater.* **2020**, *394*, 122255. [CrossRef]
76. Mcdonald-wharry, J. 2013–2014 Survey of Chars Using Raman Spectroscopy. *J. Carbon Res.* **2021**, *7*, 63. [CrossRef]
77. Inoue, J.; Yoshie, A.; Tanaka, T.; Onji, T.; Inoue, Y. Disappearance and alteration process of charcoal fragments in cumulative soils studied using Raman spectroscopy. *Geoderma* **2017**, *285*, 164–172. [CrossRef]
78. Pusceddu, E.; Montanaro, A.; Fioravanti, G.; Santilli, S.F.; Foscolo, P.U.; Criscuoli, I.; Raschi, A.; Miglietta, F. Comparison between Ancient and Fresh Biochar Samples, A Study on The Recalcitrance of Carbonaceous Structures During Soil Incubation. *Int. J. New Technol. Res.* **2017**, *3*, 39–46.
79. Feng, D.; Zhao, Y.; Zhang, Y.; Sun, S.; Gao, J. Steam Gasification of Sawdust Biochar Influenced by Chemical Speciation of Alkali and Alkaline Earth Metallic Species. *Energies* **2018**, *11*, 205. [CrossRef]
80. Wu, Y.; Sun, Y.; Liang, K.; Yang, Z.; Tu, R.; Fan, X.; Cheng, S.; Yu, H.; Jiang, E.; Xu, X. Enhancing Hydrodeoxygenation of Bio-oil via Bimetallic Ni-V Catalysts Modified by Cross-Surface Migrated-Carbon from Biochar. *ACS Appl. Mater. Interfaces* **2021**, *13*, 21482–21498. [CrossRef]
81. Chen, Y.; Cui, Z.; Ding, H.; Wan, Y.; Tang, Z.; Gao, J. Cost-Effective Biochar Produced from Agricultural Residues and Its Application for Preparation of High Performance Form-Stable Phase Change Material via Simple Method. *Int. J. Mol. Sci.* **2018**, *19*, 3055. [CrossRef]
82. Riva, L.; Cardarelli, A.; Andersen, G.J.; Buø, T.V.; Barbanera, M.; Bartocci, P.; Fantozzi, F.; Nielsen, H.K. On the self-heating behavior of upgraded biochar pellets blended with pyrolysis oil: Effects of process parameters. *Fuel* **2020**, *278*, 118395. [CrossRef]
83. Wang, B.; Xu, M.; Chi, C.; Wang, C.; Meng, D. Degradation of methyl orange using dielectric barrier discharge water falling film reactor. *J. Adv. Oxid. Technol.* **2017**, *20*, 20170021. [CrossRef]
84. Xu, J.; Sun, M.; Zhang, C.; Wu, M.; Fu, D. Electrochemical mineralization of direct blue 71 with boron-doped diamond anodes: Factor analysis and mechanisms study. *J. Environ. Chem. Eng.* **2022**, *10*, 107031. [CrossRef]
85. Yaghoot-nezhad, A.; Saebnoori, E.; Danaee, I.; Elahi, S.; Bahrami, N.; Khosravi-nikou, M.R. Evaluation of the oxidative degradation of aromatic dyes by synthesized nano ferrate (VI) as a simple and effective treatment method. *J. Water Process Eng.* **2022**, *49*, 103017. [CrossRef]
86. Shahzad, K.; Najam, T.; Bashir, M.S.; Nazir, M.A.; ur Rehman, A.; Bashir, M.A.; Shah, S.S.A. Fabrication of Periodic Mesoporous Organo Silicate (PMOS) composites of Ag and ZnO: Photo-catalytic degradation of methylene blue and methyl orange. *Inorg. Chem. Commun.* **2021**, *123*, 108357. [CrossRef]
87. Shan, R.; Lu, L.; Gu, J.; Zhang, Y.; Yuan, H.; Chen, Y.; Luo, B. Photocatalytic degradation of methyl orange by Ag/TiO2/ biochar composite catalysts in aqueous solutions. *Mater. Sci. Semicond. Process.* **2020**, *114*, 105088. [CrossRef]
88. Lu, L.; Shan, R.; Shi, Y.; Wang, S.; Yuan, H. A novel TiO_2/biochar composite catalysts for photocatalytic degradation of methyl orange. *Chemosphere* **2019**, *222*, 391–398. [CrossRef]
89. Ren, Y.; Liu, X.; Li, H.; Wang, X.; Jing, X. Synthesis and visible light photocatalytic performance of HC/BiOBr/ Bi12TiO20 microspheres. *Chem. Phys. Lett.* **2022**, *797*, 139584. [CrossRef]
90. Wang, Z.; Li, Y.; Xie, X.; Wang, Z. Bifunctional $MnFe_2O_4$/ chitosan modified biochar composite for enhanced methyl orange removal based on adsorption and photo-Fenton process. *Colloids Surfaces A Physicochem. Eng. Asp.* **2021**, *613*, 126104. [CrossRef]
91. Bhakta, A.K.; Snoussi, Y.; El Garah, M.; Ammar, S.; Chehimi, M.M. Brewer's Spent Grain Biochar: Grinding Method Matters. *J. Carbon Res.* **2022**, *8*, 46. [CrossRef]
92. Wang, J.; Odinga, E.S.; Zhang, W.; Zhou, X.; Yang, B.; Waigi, M.G.; Gao, Y. Polyaromatic hydrocarbons in biochars and human health risks of food crops grown in biochar-amended soils: A synthesis study. *Environ. Int.* **2019**, *130*, 104899. [CrossRef]
93. Yao, Y.; Hu, H.; Zheng, H.; Hu, H.; Tang, Y.; Liu, X.; Wang, S. Nonprecious bimetallic Fe, Mo-embedded N-enriched porous biochar for efficient oxidation of aqueous organic contaminants. *J. Hazard. Mater.* **2022**, *422*, 126776. [CrossRef]

94. Wang, R.; Huang, D.; Liu, Y.; Zhang, C.; Lai, C.; Wang, X.; Gong, X.-M.; Zeng, G.-M.; Duan, A.; Xu, P.; et al. Recent advances in biochar-based catalysts: Properties, applications and mechanisms for pollution remediation. *Chem. Eng. J.* **2019**, *371*, 380–403. [CrossRef]
95. Chu, J.; Kang, J.; Park, S.; Lee, C. Application of magnetic biochar derived from food waste in heterogeneous sono-Fenton-like process for removal of organic dyes from aqueous solution. *J. Water Process Eng.* **2020**, *37*, 101455. [CrossRef]